# 3D core kinematics of NGC 6362: central rotation in a dynamically evolved globular cluster

Emanuele Dalessandro [1]★ Silvia Raso,[1] Sebastian Kamann [2] Michele Bellazzini [1]
Enrico Vesperini,[3] Andrea Bellini[4] and Giacomo Beccari [5]

[1]*INAF - Osservatorio di Astrofisica e Scienza dello Spazio di Bologna, Via Gobetti 93/3, Bologna I-40129, Italy*
[2]*Astrophysics Research Institute, Liverpool John Moores University, 146 Brownlow Hill, Liverpool L3 5RF, UK*
[3]*Department of Astronomy, Indiana University, Swain West, 727 E. 3rd Street, Bloomington, IN 47405, USA*
[4]*Space Telescope Science Institute, 3700 San Martin Drive, Baltimore, MD 21218, USA*
[5]*European Souther Observatory, Karl Schwarzschild Strasse 2, D-85748 Garching bei Munchen, Germany*

## ABSTRACT

We present a detailed 3D kinematic analysis of the central regions ($R < 30$ arcsec) of the low mass and dynamically evolved galactic globular cluster (GC) NGC 6362. The study is based on data obtained with ESO-VLT/MUSE used in combination with the adaptive optics module and providing ∼3000 line-of-sight radial velocities, which have been complemented with *Hubble Space Telescope* proper motions. The quality of the data and the number of available radial velocities allowed us to detect for the first time a significant rotation signal along the line of sight in the cluster core with amplitude of ∼1 km s$^{-1}$ and with a peak located at only ∼20 arcsec from the cluster centre, corresponding to only ∼10 per cent of the cluster half-light radius. This result is further supported by the detection of a central and significant tangential anisotropy in the cluster innermost regions. This is one of the most central rotation signals ever observed in a GC to date. We also explore the rotational properties of the multiple populations hosted by this cluster and find that Na-rich stars rotate about two times more rapidly than the Na-poor sub-population thus suggesting that the interpretation of the present-day GC properties require a multicomponent chemo-dynamical approach. Both the rotation amplitude and peak position would fit qualitatively the theoretical expectations for a system that lost a significant fraction of its original mass because of the long-term dynamical evolution and interaction with the Galaxy. However, to match the observations more quantitatively further theoretical studies to explore the initial dynamical properties of the cluster are needed.

**Key words:** techniques: photometric – techniques: spectroscopic – astrometry – Hertzsprung–Russell and colour–magnitude diagrams – stars: kinematics and dynamics – globular clusters: individual: NGC6362.

## 1 INTRODUCTION

Globular clusters (GCs) are true touchstones for Astrophysics. Their study can bring crucial information on a variety of subjects ranging from stellar evolution (Cassisi & Salaris 2013) to the initial epochs of star formation in the Universe and eventually to the formation and mass assembly history of their host galaxies (e.g. Brodie & Strader 2006; Dalessandro et al. 2012; Forbes et al. 2018; Krumholz, McKee & Bland-Hawthorn 2019).

Traditionally, GCs have been considered as relatively simple spherical, non-rotating, and almost completely relaxed systems. However, observational results obtained in the past few years are demonstrating that they are much more complex than previously thought. In particular, the classical simplified approach of neglecting rotation in GCs has become untenable from the observational point of view. In fact, there is an increasing wealth of observational results suggesting that, when properly surveyed, the majority of GCs rotate at some level. As of today, more than 50 per cent of the sampled

GCs show clear signatures of internal rotation (e.g. Anderson & King 2003; Bellazzini et al. 2012; Fabricius et al. 2014; Bianchini et al. 2018; Ferraro et al. 2018; Kamann et al. 2018a; Lanzoni et al. 2018a,b; Sollima, Baumgardt & Hilker 2019). Moreover, evidence of rotation has also been reported for intermediate-age clusters (Mackey et al. 2013; Kamann et al. 2018b), young massive clusters (Hénault-Brunet et al. 2012; Dalessandro et al. 2021), and nuclear star clusters (Nguyen et al. 2018; Neumayer, Seth & Böker 2020) indicating that internal rotation is a common ingredient across dense stellar systems of different sizes and ages. On the theoretical side, the presence of internal rotation has strong implications on our understanding of the formation and dynamics of GCs and affects, for example, their long-term evolution (Einsel & Spurzem 1999; Ernst et al. 2007; Breen, Varri & Heggie 2017) and their present-day morphology (e.g. Hong et al. 2013; van den Bergh 2008). Moreover, signatures of internal rotation could be crucial in revealing the formation mechanisms of the so-called multiple stellar populations (MPs) in GCs (Bekki 2010; Mastrobuono-Battisti & Perets 2013; Hénault-Brunet et al. 2015) differing in terms of their light-element (such as He, Na, O, C, N) abundances (see Bastian & Lardo 2018; Gratton et al. 2019

★ E-mail: emanuele.dalessandro@inaf.it

for recent reviews on the subject), and which are observed in almost all GCs now. Differences in the rotation amplitudes of MPs have been observed in two cases so far, namely M 13 and M 80 (Cordero et al. 2017; Kamann et al. 2020)[1] and in both clusters the Na-rich population (also known as second population or generation – SP) is found to rotate with a larger amplitude than the first population FP (Na-poor).

In general, GCs are characterized by moderate rotation, with typical ratios of rotational velocities to central velocity dispersions ($V_{rot}/\sigma_0$) ranging from about 0.05 to about 0.6 (Bellazzini et al. 2012; Fabricius et al. 2014). However, the present-day rotation in GCs is likely the remnant of a stronger early rotation (see e.g. Hénault-Brunet et al. 2012; Mapelli 2017) gradually weakened by the effects of two-body relaxation (Bianchini et al. 2018; Kamann et al. 2018a; Sollima et al. 2019). In fact, recent *N*-body simulations (Hong et al. 2013; Tiongco, Vesperini & Varri 2017) provide evidence that during the cluster long-term evolution, the amplitude of the rotation decreases due to angular momentum redistribution and star escape. At the same time, the peak of the rotation curve gradually moves towards the cluster innermost regions.

As a part of a project aimed at studying the structural and kinematical properties of GCs and their MPs (e.g. Dalessandro et al. 2014, 2018a,b, 2019; Massari et al. 2016; Kamann et al. 2020), our group is conducting a thorough investigation of the low-mass Galactic GC NGC 6362 ($M \sim 5 \times 10^4 \, M_\odot$). Based on a combination of spectro-photometric observations, our previous analyses suggest (Dalessandro et al. 2014, 2018a; Mucciarelli et al. 2016; Massari et al. 2017) that the cluster underwent severe mass loss due to long-term dynamical evolution and quite strong interaction with the Galaxy (Miholics, Webb & Sills 2015; Kundu et al. 2019). In fact, we find that FP and SP stars have indistinguishable radial distributions allover the cluster extension, as expected for a cluster in an advanced dynamical stage (Vesperini et al. 2013; Dalessandro et al. 2019). In addition, the velocity dispersion profiles of the two sub-populations show differences of the order of $\sim$1 km s$^{-1}$ at intermediate/large cluster-centric distances that can be ascribed to the combined effects of advanced dynamical evolution and a significantly larger FP binary fraction with respect to the SP one that can inflate the velocity dispersion by the observed amount (Dalessandro et al. 2018a). The hypothesis of an advanced dynamical state of the cluster is also supported by the quite flat mass function of the system (Paust et al. 2010). In Dalessandro et al. (2018a), we also verified that NGC 6362 does not show any significant evidence of large-scale line-of-sight rotation ($V_{rot} \sim 0.17^{+0.32}_{-0.17}$ km s$^{-1}$) as also confirmed by Bianchini et al. (2018) and Sollima et al. (2019) by using Gaia DR2 proper motions (PM).

Here, we perform a 3D kinematic analysis of the innermost region ($R < 30$ arcsec) of the cluster, which was only poorly sampled by previous observational campaigns. To this aim, we use a combination of proprietary MUSE deep data supported by adaptive optics, and *HST* PMs published in previous works. The paper is structured as follows. The observational data set and data analysis are presented in Section 2, while in Section 3, we define the sample of stars used to perform the kinematic analysis. Section 4 details on the kinematic analysis and derived results and Section 5 focuses on the relative kinematics of MPs. Conclusions are discussed in Section 6.

---

[1]Differential rotation among different populations were also observed in $\omega$ Centauri (Bellini et al. 2018). However, it is important to stress that the star formation history of this system is by far not typical for GCs and its sub-populations differ also in terms of age and metallicity.
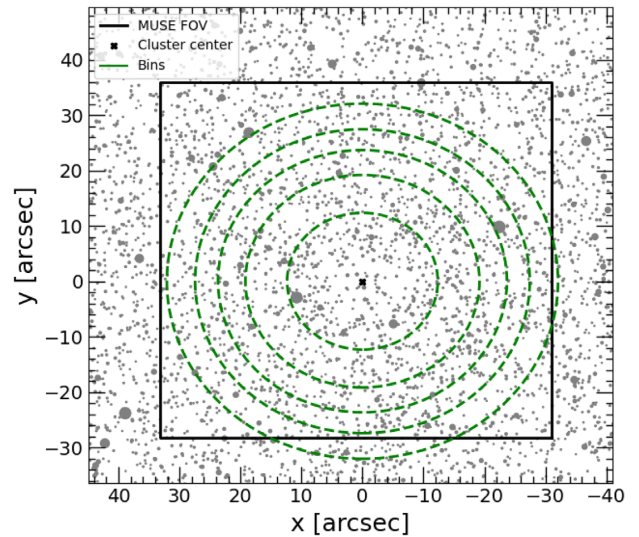
**Figure 1.** Footprint of the MUSE observations (black box). Green circles represent the bins used for the kinematic analysis, while the black cross is the cluster centre from Dalessandro et al. (2014).

## 2 OBSERVATIONS AND DATA ANALYSIS

The main observational data set used in this work consists of MUSE@ESO-VLT data obtained with the support of the adaptive optics module GALACSI (Prop ID: 0103.D-0545; PI: Dalessandro). Two Wide Field Mode pointings, epoch A and B, respectively, both centred on the cluster (Fig. 1) and with exposure time of 2400 s each, were obtained between 2019 May 1 and 2. Each pointing was observed with four different instrument derotator angles (0°, 90° and 180°, 270°) in order to level out possible resolution differences between the individual spectrographs. The data cubes were reduced by using the standard MUSE pipeline (Weilbacher et al. 2020). An average full width at half-maximum (FWHM) of $\sim$0.7 arcsec was delivered by the system for each pointing, whereas the uncorrected FWHM (i.e. seeing) during the observations was $\sim$1.0 arcsec.

Stellar spectra were extracted from the reduced data cubes using PAMPSELMUSE (Kamann, Wisotzki & Roth 2013; Kamann 2018). Besides the integral-field data, the software requires a photometric reference catalogue as input. To this aim, we used the *HST* multiband photometric catalogue presented in Dalessandro et al. (2014). PAM-PELMUSE fits a wavelength-dependent PSF as well as a coordinate transformation from the reference *HST* catalogue to the MUSE data and uses this information to optimally extract the spectra of the resolved sources. The same analysis was performed on both the cubes created for the individual epochs and on the cube using all available exposures.

At the end of the analysis, we extracted 2 658 individual stellar spectra for epoch A and 2 650 individual stellar spectra for epoch B. While from the combined cube we were able to derive 2 925 spectra.

The extracted spectra were cross-correlated against synthetic templates from the GLib library (Husser et al. 2013) to derive 'first-pass' line-of-sight radial velocities (LOS-RVs). For each extracted spectrum, a matching template was selected based on the effective temperature and surface gravity values derived photometrically for the corresponding star, via a comparison with an isochrone. We used a BaSTI (Pietrinferni et al. 2006) $\alpha$-enhanced theoretical model with adequate metallicity ([Fe/H] $= -1.09$; Mucciarelli et al. 2016; Massari et al. 2017; Dalessandro et al. 2018a) and with age $t = 12.5$ Gyr (Dotter et al. 2010). In the final step of the analysis,
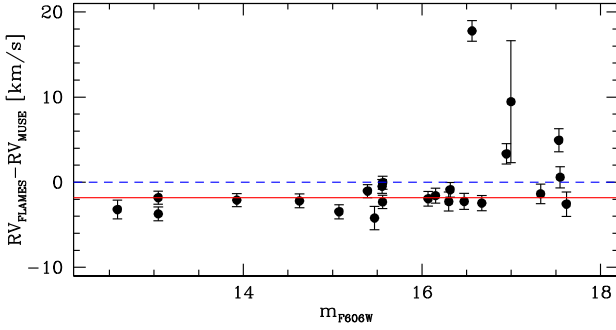
**Figure 2.** Difference between the FLAMES and MUSE radial velocities as a function of the F606W magnitude (black circles). The MUSE radial velocities are obtained from the full spectral fit. The blue dashed line corresponds to 0, while the red solid line corresponds to the median value of the difference between the two velocities.

we performed a full-spectrum fit of each spectrum, using the `Spexxy` tool (Husser et al. 2016). In addition to the aforementioned effective temperatures and surface gravities, we used in this step also the first-pass LOS-RVs as initial guesses for the fit. Given the low spectral resolution of the MUSE data, the surface gravities were held fixed at their initial guesses, while leaving the LOS-RVs, effective temperatures, and metallicities of the stars as free parameters.

In addition to the MUSE catalogue, we used two complementary data sets. We made use of the FLAMES data presented in Dalessandro et al. (2018a), which cover the entire extension of the cluster out to a distance of R ∼ 800 arcsec from its centre and provide high-resolution LOS-RVs for 489 cluster members selected based on both their velocities and metallicities (see Dalessandro et al. 2018a for details). We point out here that while covering a larger field of view than MUSE, the FLAMES catalogue is significantly shallower and it includes only stars with $m_{F606W} < 17.7$. We checked for possible radial velocity systematic differences between the MUSE and FLAMES samples by using the 24 stars in common between the two data sets. In Fig. 2, we show the difference between the FLAMES and MUSE LOS-RVs as a function of the $m_{F606W}$ magnitude. The median value of the difference results to be $RV_{FLAMES} - RV_{MUSE} \sim -1.9$ km s$^{-1}$. For comparison, the median value of the combined radial velocity errors for the stars in common between the two data sets, is ∼1 km s$^{-1}$. To homogenize the two samples, and because of the larger resolution of FLAMES, we applied to all the MUSE LOS-RVs a shift equal to the derived median difference in radial velocity.

Finally, to study the cluster core kinematics also on the plane of the sky thus enabling a 3D view, we used the *HST* PM catalogue published by Bellini et al. (2014). We refer the reader to that papers for details about the analysis and PM derivation. Here, we just note that the PM catalogue extends up to distances $R \sim 100$ arcsec from the cluster centre, thus totally including the MUSE field of view, and it also samples stars in a similar luminosity range as MUSE.

## 3 SAMPLE SELECTION

For the kinematic analysis of the MUSE data set, we used the LOS-RVs derived by means of the full spectrum analysis and obtained from the combined cube. As shown in Fig. 3, the full sample covers a wide range of ∼13 magnitudes ($12 < m_{F606W} < 25$) and as consequence of signal-to-noise (S/N) ratios, which in turn range from ∼200 to
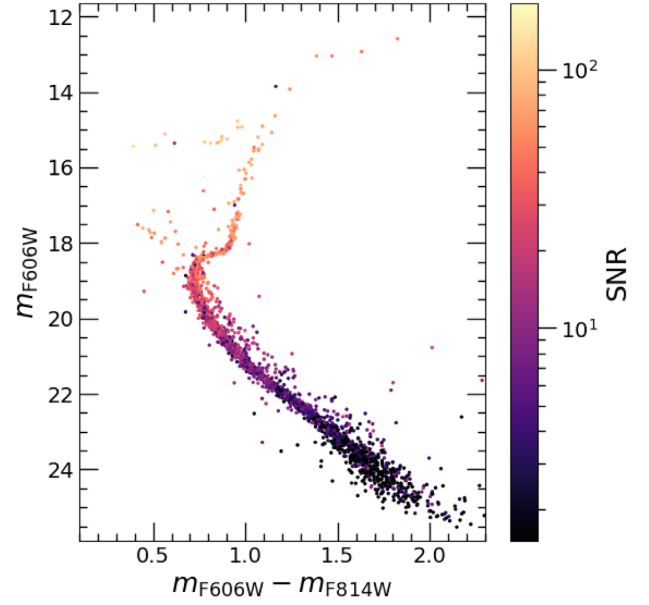


**Figure 3.** $m_{F606W} - m_{F814W}$ versus $m_{F606W}$ colour-magnitude-diagram of all the stars in the MUSE catalogue. Each star is colour coded according to the S/N ratio of the corresponding spectrum (see colorbar on the right side of the figure).

∼2. Since our goal is to derive kinematic quantities that are expected to have relatively small amplitudes and to compare the kinematic properties of different sub-populations in the cluster, we adopted rather strict selection criteria to avoid contamination from spurious signals of any origin.

First, we excluded all stars with $S/N < 15$, which roughly corresponds to a magnitude selection $m_{F606W} < 19.5$. Then, similarly to what done in Kamann et al. (2018a), we adopted also the following selection criteria: (i) we defined a magnitude accuracy (*acc.*) as in section 4.4 of Kamann et al. (2018a), and excluded stars with $acc. \leq 0.8$. This cut allows us to exclude stars whose LOS-RV is potentially contaminated from bright neighbours; (ii) we excluded stars with a *r*-parameter ($r_{cc}$ - Tonry & Davis 1979), which indicates the reliability of each cross-correlation measurement, $r_{cc} \leq 4$; (iii) we measured the difference between the LOS-RVs obtained with the cross-correlation and with the full spectrum fit ($\Delta v$), and we rejected all the stars for which this difference was larger than three times the combined uncertainty of the two radial velocities measurements; (iv) we excluded stars that, at each given magnitude, have a LOS-RV error ($\epsilon_{RV}$) larger than 3σ from the local median radial velocity error. In Fig. 4, we show the distribution of stars in the MUSE catalogue as a function of the $m_{F606W}$ magnitude and the quality parameter just described. In all panels, we represent the complete MUSE sample as grey dots, and the selected sample, satisfying the criteria listed above, as black dots.

Finally, in order to exclude potential field interlopers in the sample of LOS-RVs selected as described above, following Dalessandro et al. (2018a), we excluded stars with LOS-RVs outside the range: $-29.3$ km s$^{-1}$ < RV < $0.7$ km s$^{-1}$. The LOS-RV distribution as function of the cluster-centric distance is shown in Fig. 5 along with the adopted velocity cuts to exclude likely non-cluster members (red lines).

The final MUSE sample surviving to the above quality and membership selections and that will be used for the following kinematic analysis counts 485 stars. For comparison, with our
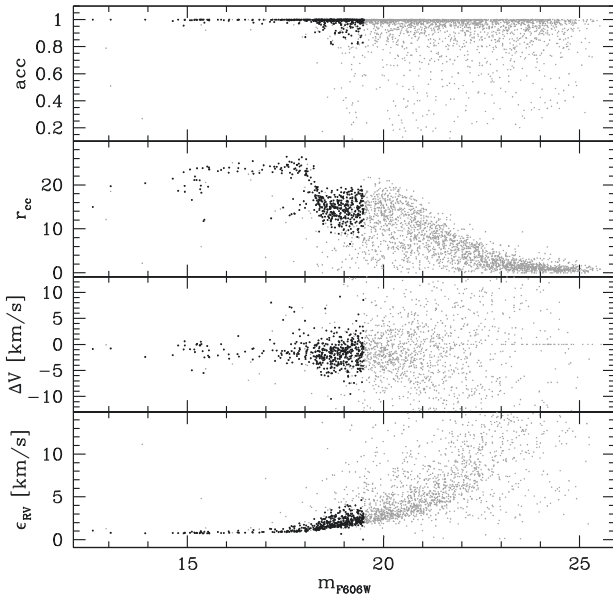
**Figure 4.** From top to bottom: magnitude accuracy, reliability of each cross-correlation measurement ($r_{cc}$), difference between the radial velocities measured with the cross-correlation and the full spectrum fit, and radial velocity error as a function of the F606W magnitude. In all panels, the complete MUSE catalogue is represented as grey dots, while the selected sample, according to the selection criteria listed in the text, is represented as black dots.
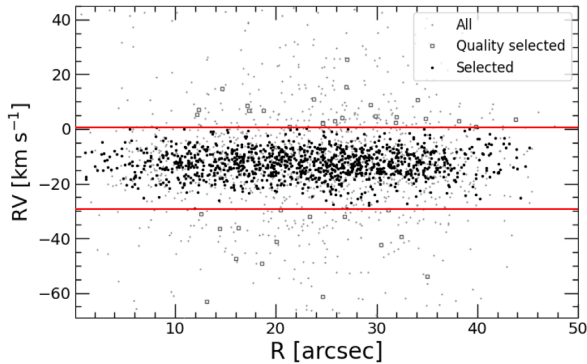


**Figure 5.** Radial velocities as a function of the distance from the cluster centre. The complete MUSE catalogue is represented as grey dots, while the selected sample is represented as black circles. The two red horizontal lines mark the radial velocity cuts adopted to exclude potential non-cluster members (from Dalessandro et al. 2018a). The open grey squares are stars that would pass our spectroscopic quality criteria, but their RV is not compatible with being cluster members.

previous screening with FLAMES, in the same field of view we were able to derive LOS-RVs for only 34 stars.

For the quality and membership selection of the FLAMES data, we recall the reader to the detailed description in Dalessandro et al. (2018a). Here, we just stress that only FLAMES targets (465) located outside the MUSE field of view will be used in the following. In total the final kinematic analysis will be based on a sample of reliable LOS-RVs of 950 bonafide cluster members.

*HST* PMs were selected by using the following criteria. Only stars that (i) at a given magnitude, have QFIT parameter smaller than the 80th percentile (the QFIT parameter indicates the quality of the PSF fit, with smaller values of this parameter indicating a better quality of

the PSF fit); ii) have PM with reduced $\chi^2$, obtained from the PM fit, smaller than 2, and iii) PM measures for which the fraction of rejected displacement measurements in the PM fit procedure is smaller than 15 per cent, were considered for the following analysis. In addition, we excluded stars with a PM larger than six times the dispersion of the PM distribution to exclude obvious non-cluster members, and stars with a magnitude in the F606W band fainter than 19.5, in order to be roughly consistent with the magnitude cut indirectly applied on the MUSE data. The final sample includes 1633 stars with reliable PMs.

## 4 KINEMATIC ANALYSIS

The kinematic analysis was performed by using the selected sample of stars in the MUSE catalogue (see Section 3) and by following the maximum-likelihood approach described by Pryor & Meylan (1993). The method is based on the assumption that the probability of finding a star with a velocity of $v_i \pm \epsilon_i$ at a projected distance from the cluster centre $R_i$ can be approximated as

$$p(v_i, \epsilon_i, R_i) = \frac{1}{2\pi \sqrt{\sigma^2 + \epsilon_i^2}} exp \frac{(v_i - v_0)^2}{-2\left(\sigma^2 + \epsilon_i^2\right)} \quad (1)$$

where $v_0$ and $\sigma$ are the systemic radial velocity and the intrinsic dispersion profile of the cluster, respectively. Rotation was included in the analysis by adding the following angular dependence (e.g. Copin et al. 2001; Krajnović et al. 2006; Kamann et al. 2018a) to the mean velocity of equation (1).

$$v_0 = v_0 + v_{rot}(R_i)sin(\theta_i - \theta_0(R_i)) \quad (2)$$

where $v_{rot}$ and $\theta_0$ represent the projected rotation velocity and the rotation axis angle respectively as a function of the projected distance R to the cluster centre. The axis angle as well as the position angle $\theta_i$ of a star are measured from north through east. We restricted the prior for $\theta_0$ to a 180° wide interval and we allowed the rotation velocity to assume both positive and negative values, in order to avoid a skewed rotation velocity probability distribution in case of very small or no rotation (see also Kamann et al. 2020). In particular, we used an iterative procedure in which we adopted an angular interval [$\alpha$; $\alpha$ + 180°) centred on the most probable rotation axis angle. This is useful to avoid skewness in the probability distribution of $\theta_0$ when its value is close to 0° or 180°. We split the sample in five concentric annuli centred on the cluster centre and with width varying in such a way that each bin contains the same number of stars (80). Only stars with $r < 32$ arcsec were considered in the analysis as they guarantee an almost complete coverage within each annulus (Fig. 1).

The fit of the kinematical quantities was performed by using EMCEE (Foreman-Mackey et al. 2013) with uniform priors, which provides the posterior probability distribution density functions (PDFs) for $\sigma$, $v_{rot}$ and $\theta_0$ in each bin. We report as best-fitting parameter the median of the marginalized posterior PDF of each parameter, and as uncertainty the interval between the 16th and 84th percentile of the marginalized posterior PDF.

The results of the analysis of the MUSE data are shown in Figs 6 and 7 as grey circles. We then complemented the MUSE data with FLAMES LOS-RVs to study the kinematics along the entire cluster extension. While the FLAMES sample is shallower than the MUSE one and includes only stars with $m_{F606W} < 17.7$, it is important to note that stars in the two data sets have approximately the same mass within ~0.05 M$_\odot$. Only stars in the FLAMES catalogue located at $R > 35$ arcsec were used and the same analysis as before was performed (white circles in Figs 6 and 7).

In Fig. 6, the resulting velocity dispersion profile is shown along with the best-fitting Plummer model obtained in Dalessandro et al.
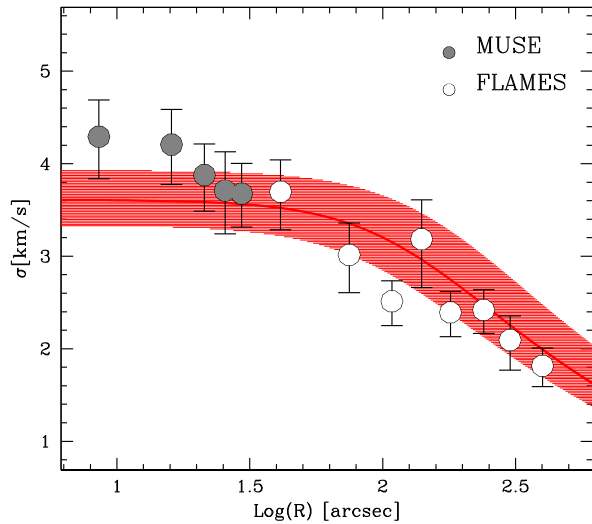
**Figure 6.** Velocity dispersion profile obtained by the combination of MUSE (grey circles) and FLAMES (white; Dalessandro et al. 2018a) data. The red line and shaded area represents the best-fitting curve and the corresponding error obtained in Dalessandro et al. (2018a).

(2018a). We note that the MUSE data show some hints of an increasing dispersion in the innermost two bins, however they are still compatible with the expected flat behaviour.

As for the rotation (Fig. 7), a significant signal is clearly visible when considering the MUSE data. In fact, the profile increases out to Log(R) $\sim$ 1.2 ($\sim$20 arcsec) from the cluster centre showing a maximum amplitude of $\sim$1.4 km s$^{-1}$. Then it tends to slowly decline moving outward. The addition of the FLAMES data confirms the smoothly declining external branch of the rotation profile. The mean rotation axis angle calculated by averaging all the single bin values results to be located approximately at $\theta_0 \sim 77° \pm 35°$, where the error is given by the standard deviation. The derived MUSE + FLAMES velocity dispersion and rotation values are reported in Table 1.

In Fig. 7, we also show the best-fitting curve of the rotational velocity radial profile, obtained imposing that it has the following analytic form, as appropriate for cylindrical rotation (Lynden-Bell 1967):

$$v_{\rm rot} = \frac{2v_{pk}R}{R_{pk}}\left(1+\left(\frac{R}{R_{pk}}\right)^2\right)^{-1} \tag{3}$$

where $R_{pk}$ and $v_{pk}$ represent the location of the rotation peak and its amplitude, respectively. The best-fitting curve was obtained by letting the values of $v_{pk}$ and $R_{pk}$ vary and by estimating the reduced $\chi^2$ of the residuals between the observed and the model profiles. The solution corresponding to the lowest value of the stored $\chi^2$ is finally adopted as the best-fitting model. The errors on these two parameters correspond to the interval where $\chi^2 \leq \chi^2_{\rm best} + 1$. The derived best-fitting values are $v_{pk} = (0.96 \pm 0.09)$ km s$^{-1}$ and $R_{pk} = (17.3^{+2.7}_{-2.8})''$.

In the lower panel of Fig. 7, we also show the $V_{rot}/\sigma$ profile that provides a direct measure of the ordered to random stellar motion. A peak at $V_{rot}/\sigma = 0.32 \pm 0.1$ is visible in this plot at the same bin as the rotation profile peak.

This result represents the first detection of rotation in NGC 6362. In addition, with a peak located at only $\sim$0.1 R$_h$ (R$_h$ = 150 arcsec; Dalessandro et al. 2014), this is one of the most central rotation signal ever observed in a GC to date. A similar case was found in the massive post-core-collapse GC M 15, which shows a decoupled rotating core (van den Bosch et al. 2006; Usher et al. 2021). Likely

the combination of a modest absolute amplitude and the very central position of the rotation peak has made the signal elusive to previous screenings.

We also note that $V_{rot}/\sigma$ tends to increase in the cluster outermost regions ($Log(R) > 2.2$). N-body simulations of the long-term evolution of GCs have shown that clusters evolve towards a state of partial spin-orbit synchronization characterized by an internal solid-body rotation with angular velocity equal to $\Omega/2$ where $\Omega$ is the angular velocity of the cluster's orbital motion around the Galactic centre (Tiongco, Vesperini & Varri 2016). In the lower panel of Fig. 7, we have plotted three radial profiles for $V_{rot}/\sigma$ with $V_{rot}$ calculated assuming a solid-body rotation with angular velocities $\Omega_p/2$, $\Omega_a/2$, and $\Omega_e/2$ calculated by simply assuming $V_{circ} = 220$ km s$^{-1}$ and Galactocentric distances equal to, respectively, the cluster's pericentre ($R_p = 2.54$ kpc), apocentre ($R_a = 5.16$ kpc), and effective Galactocentric distance ($R_e = R_a(1-e)$ where $e = 0.35$ is the orbital eccentricity; see Baumgardt et al. 2019). The solid-body rotation profiles shown in Fig. 7 suggest that the outer kinematic properties revealed by our data might represent the signature of the cluster's partial spin-orbit synchronization. Additional data allowing a firmer determination of the cluster's outer kinematics along with specific models aimed at modelling the kinematic evolution of NGC 6362 are however necessary to further explore this issue.

### 4.1 Proper motion analysis

We also studied the kinematics of the central regions of NGC 6362 in the plane of the sky by using the PM catalogue described in Sections 2 and 3 for stars with $m_{F606W} < 19.5$. We stress here that because of the way PMs are derived, it is not possible to quantitatively study the rotation as it is (at least partially) erased by the linear transformations necessary to report all catalogues on the same astrometric reference frame. However, some residuals can be expected to be still imprinted along the tangential component of the motion.

We divided the selected PM sample into six equally populated (270 stars per bin) radial bins. In each bin, we derived the velocity dispersions in both the tangential and radial components by using again a maximum likelihood approach and the EMCEE (Foreman-Mackey et al. 2013) algorithm to obtain the posterior PDFs for the tangential and radial components of the velocity dispersion $\sigma_{\rm tan}$ and $\sigma_{\rm rad}$, respectively (see Raso et al. 2020 for more details).

The results of this analysis are summarized in Fig. 8. The anisotropy profile (defined here as $\sigma_{tan}/\sigma_{rad}$) shows clear evidence of an excess of motion along the tangential component in the innermost $30-40$ arcsec. Indeed, the innermost three radial bins have an average anisotropy value $< \sigma_{tan}/\sigma_{rad} > = 1.16 \pm 0.02$ and each of the three measures exceeds the isotropic behaviour by $\sim$2$\sigma$. We note that a hint of central tangential anisotropy was also found by Watkins et al. (2015). This behaviour is in qualitative agreement with what expected based on the central rotation observed with MUSE LOS-RVs.

To perform a one-to-one comparison with the MUSE results, we repeated the analysis including only stars (453) in common with the selected MUSE catalogue. Also in this case, the PM analysis reveals a consistent indication of tangential anisotropy in the innermost regions of the cluster although the distribution results to be noisier because of the lower number statistics.

### 4.2 Ellipticity

A rotating system is also expected to be flattened in the direction perpendicular to the rotation axis (Chandrasekhar 1969). We used the *HST* catalogue from Dalessandro et al. (2014) to construct a 2D
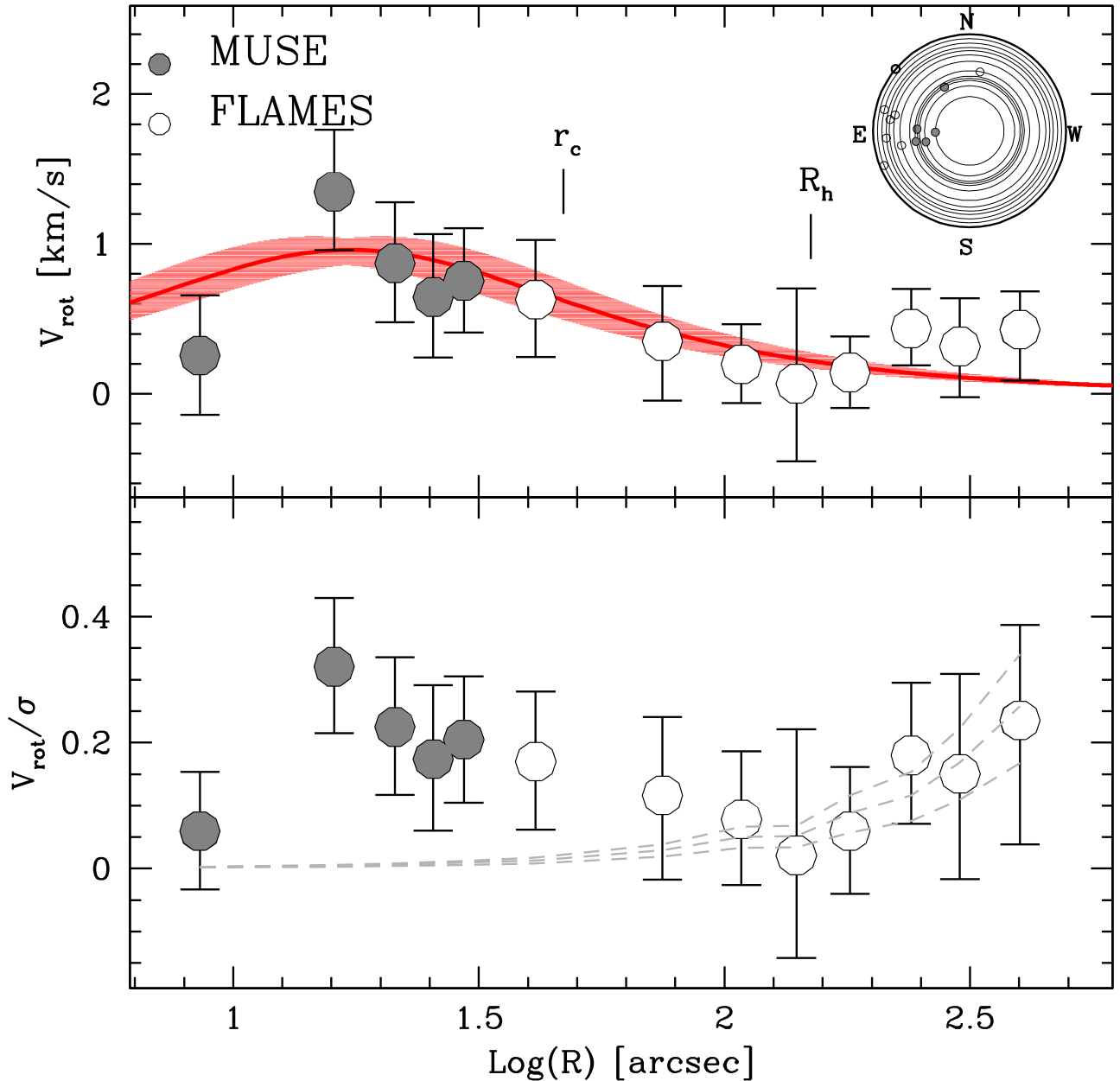
**Figure 7.** Upper panel: Rotational velocity and rotation axis (inset) angle as a function of the distance from the centre. The red line and shaded area represents the best-fitting curve and the corresponding error, obtained as described in Section 4. The core and half-light radii are also marked, for reference. Lower panel: $V_{rot}/\sigma$ profile. An excess reaching values of $V_{rot}/\sigma \sim 0.3$ is present in the central regions also in this case. Grey dashed lines represent the solid-body rotation profiles obtained by assuming partial spin-orbit synchronisation at three Galactocentric distances (see discussion in Section 4).

density map of the cluster central regions and study its morphology. The 2D density map shown in Fig. 9 (lower panel) was obtained by transforming the distribution of stars $m_{F606W} < 25$ into a smoothed surface density function through the use of a Gaussian kernel with width of 5 arcsec. To minimize the effect of the limited field of view on the smoothing procedure, the analysis was limited to an area of $\sim 85 \times 85$ arcsec$^2$. The lower panel of Fig. 9 also shows the best-fitting ellipses to the isodensity contours. The distribution of their ellipticity $\epsilon = 1 - b/a$, where $a$ and $b$ are the major and minor axis, respectively, as a function of the cluster-centric distance are shown in the upper panel and reported in Table 2. As apparent, the ellipticity is more prominent in the innermost rotating regions and it reaches its maximum ($\epsilon = 0.20 \pm 0.02$) at $R \sim 20$ arcsec. Then ellipticity progressively smooths out moving outward. In fact, in the outermost

regions $\epsilon = 0.1 \pm 0.02$, consistently with what found at larger distances (see for example Harris 1996). The ellipses major axis tend to have an orientation of $\sim 160°$ in the north-east direction and the stellar density distribution is flattened in the direction of the average position angle of the rotation axis consistent, in general, with the expectation for a system flattened by its internal rotational velocity.

## 5 KINEMATICS OF MULTIPLE POPULATIONS

MPs are believed to form during the very early epochs of GC formation and evolution (10–100 Myr). A number of scenarios have been proposed over the years to explain their formation, however their origin is still strongly debated (Decressin, Charbonnel & Meynet

**Table 1.** MUSE + FLAMES velocity dispersion and rotation profiles.

| R (arcsec) | $\sigma$ (km s$^{-1}$) | $V_{rot}$ (km s$^{-1}$) | $\theta_0$ (degrees) |
|---|---|---|---|
| 8.5 | $4.29^{+0.45}_{-0.40}$ | $0.25^{+0.40}_{-0.40}$ | $92^{+60}_{-56}$ |
| 16.0 | $4.21^{+0.43}_{-0.38}$ | $1.35^{+0.39}_{-0.41}$ | $104^{+24}_{-24}$ |
| 21.3 | $3.88^{+0.39}_{-0.34}$ | $0.87^{+0.39}_{-0.41}$ | $30^{+44}_{-37}$ |
| 25.5 | $3.71^{+0.47}_{-0.42}$ | $0.65^{+0.40}_{-0.42}$ | $88^{+62}_{-59}$ |
| 29.5 | $3.68^{+0.36}_{-0.33}$ | $0.75^{+0.34}_{-0.35}$ | $101^{+40}_{-42}$ |
| 41.3 | $3.69^{+0.41}_{-0.34}$ | $0.63^{+0.38}_{-0.40}$ | $-10^{+47}_{-58}$ |
| 74.8 | $3.01^{+0.41}_{-0.34}$ | $0.35^{+0.40}_{-0.37}$ | $102^{+65}_{-47}$ |
| 108.3 | $2.51^{+0.26}_{-0.22}$ | $0.20^{+0.26}_{-0.27}$ | $78^{+52}_{-70}$ |
| 140.1 | $3.18^{+0.52}_{-0.43}$ | $0.07^{+0.51}_{-0.63}$ | $82^{+62}_{-76}$ |
| 180.0 | $2.39^{+0.26}_{-0.23}$ | $0.14^{+0.24}_{-0.24}$ | $95^{+59}_{-52}$ |
| 239.9 | $2.42^{+0.25}_{-0.22}$ | $0.43^{+0.25}_{-0.27}$ | $76^{+45}_{-57}$ |
| 301.5 | $2.09^{+0.32}_{-0.26}$ | $0.31^{+0.34}_{-0.32}$ | $112^{+82}_{-46}$ |
| 399.5 | $1.81^{+0.23}_{-0.19}$ | $0.43^{+0.33}_{-0.25}$ | $50^{+31}_{-96}$ |

For each annulus, the table lists the the mean radius (R), the velocity dispersion ($\sigma$), the rotation velocity ($V_{rot}$), the position angle ($\theta_0$), and relative errors.
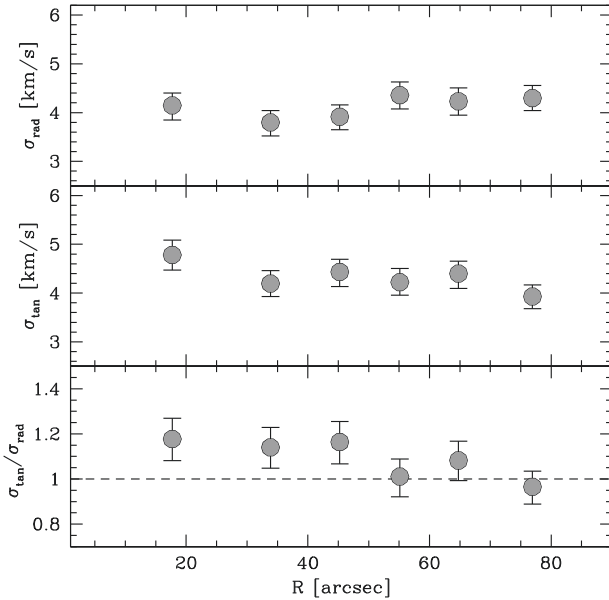
**Figure 8.** Kinematic analysis in the plane of the sky as obtained by using the quality selected PM sample and dividing it into six equally populated bins. From top to bottom: radial and tangential components of the velocity dispersion in the plane of the sky and anisotropy profile, obtained as the ratio between the tangential and radial components. The dashed line in the bottom panel marks isotropy.

2007; D'Ercole et al. 2008; Bastian et al. 2013; Denissenkov & Hartwick 2014; Gieles et al. 2018; Calura et al. 2019). It has been shown that the kinematical and structural properties of MPs can provide key insights into the early epochs of GC evolution and formation. In fact, one of the predictions of MP formation models (see e.g. D'Ercole et al. 2008) is that SP stars form a centrally segregated stellar sub-system possibly characterized by a more rapid internal rotation (Bekki 2011) than the more spatially extended FP system. Although the original structural and kinematical differences between FP and SP stars are gradually erased during GC long-term dynamical evolution (see e.g. Vesperini et al. 2013; Hénault-Brunet et al. 2015; Tiongco, Vesperini & Varri 2019), some clusters are
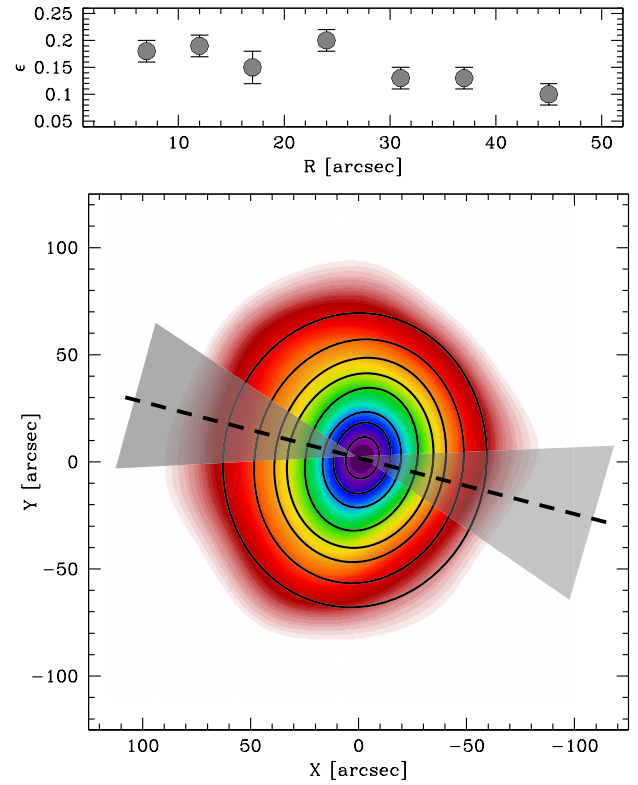
**Figure 9.** Lower panel: smoothed stellar density map of the inner 85 × 85 arcsec$^2$ of NGC 6362, obtained from *HST* photometry. The solid black lines represent the best-fitting ellipses to the isodensity curves, the dashed lines represents the average rotation axis obtained from the kinematic analysis and the shaded area the relative uncertainties. Upper panel: ellipticity distribution as a function of the cluster-centric distance.

expected to still retain some memory of these initial differences in their present-day properties (e.g. Richer et al. 2013; Bellini et al. 2015; Dalessandro et al. 2016, 2018b, 2019; Cordero et al. 2017; Kamann et al. 2020). Therefore connecting the kinematic and chemical properties of multiple populations in GCs may offer a valid approach for understanding how they formed.

The kinematic properties of NGC 6362 MPs have been investigated in detail in Dalessandro et al. (2018a). At odds with the expectations for a dynamically evolved cluster whose MPs share the same radial distributions (Dalessandro et al. 2014), we found that at distances from the cluster centre larger than about $0.5\,R_h$, FP and SP stars show hints of different line-of-sight velocity dispersion profiles, with FP stars being dynamically hotter. This effect is likely due to a significant difference of the relative binary fraction of FP (∼15 per cent) and SP (∼1 per cent) stars. On the contrary, we did not find any evidence of different rotation between the two populations. Here, we take advantage of the exquisite MUSE performance and the large sample of stars with available LOS-RVs in the innermost 30 arcsec to investigate this aspect further.

In order to separately analyse the two populations of NGC 6362, corresponding to different chemical abundances, we cross-correlated the positions and magnitudes of stars in our MUSE catalogue with the ones from the *HST* UV Legacy Survey of Galactic GCs[2] (Piotto et al. 2015; Nardiello, Libralato & Piotto G. et al. 2018). UV bands are efficient in separating MPs in colour-magnitude-diagrams (CMDs),

[2]Catalogues available at http://groups.dfa.unipd.it/ESPG/treasury.php.

**Table 2.** Ellipticity profile.

| R (arcsec) | $\epsilon$ | $\sigma_\epsilon$ | Orientation (degrees) |
|---|---|---|---|
| 7 | 0.18 | 0.02 | $155 \pm 15$ |
| 12 | 0.19 | 0.02 | $157 \pm 13$ |
| 17 | 0.15 | 0.03 | $165 \pm 13$ |
| 24 | 0.20 | 0.02 | $165 \pm 12$ |
| 31 | 0.13 | 0.02 | $162 \pm 14$ |
| 37 | 0.13 | 0.02 | $160 \pm 15$ |
| 45 | 0.10 | 0.02 | $160 \pm 15$ |

For each annulus, the table lists the mean radius (R), the ellipticity value ($\epsilon$), the orientation of the ellipse major axis, and relative errors.

as variations of the OH, CN, and CH molecular bands have strong effects in the spectral range 3000–4000 Å (Sbordone et al. 2011). Using the F275W, F336W, F438W magnitudes, combined with the F814W band, we constructed adequate colour–colour diagrams to distinguish between FP and SP stars along the red giant branch (RGB), sub-giant branch (SGB), and main sequence (MS; Milone et al. 2020). In particular, we divided our sample into three $m_{F814W}$ magnitude bins, separated at $m_{F814W} = 18.1$ and $m_{F814W} = 19.3$ thus separating the RGB, SGB, and MS. For the RGB and MS, we constructed the so-called 'chromosome map' (Milone et al. 2017) defined as the ($m_{F275W} - m_{F814W}$, $C_{F275W, F336W, F438W} = (m_{F275W} - m_{F336W}) - (m_{F336W} - m_{F438W})$) colour–colour diagram. Briefly, we verticalized the star distribution in the $m_{F814W}$ versus $C_{F275W, F336W, F438W}$ pseudo-CMD and in the $m_{F814W}$ versus $m_{F275W} - m_{F814W}$ CMD with respect to two fiducial lines at the blue and red edges of the sequence. The chromosome map corresponds to the combination of the two verticalized distributions. For the SGB, we instead constructed the $m_{F336W} - m_{F438W}$ versus $m_{F275W} - m_{F336W}$ colour–colour diagram. In the appropriate diagram for each bin, the star distribution appears to be bimodal and therefore the two populations can be easily separated.

In Fig. 10, we show the ($m_{F814W}$, $m_{F606W} - m_{F814W}$) CMD (left-hand panel) and the ($m_{F814W}$, $C_{F275W, F336W, F438W}$) pseudo-CMD (right-hand panel), where we highlight FP stars in green and SP stars in orange.

For the FLAMES data set, FP and SP stars were separated by using the Na abundances obtained in Mucciarelli et al. (2016) and Dalessandro et al. (2018a) and using a separation limit at [Na/Fe] = 0.05 (stars with [Na/Fe] < 0.05 are classified as FP, while Na-rich stars ar SP). The nice match between UV colour separation and [Na/Fe] abundances was also shown in detail in those papers.

We then repeated the kinematic analysis described in Section 4 for the FP and SP sub-populations separately. We reduced the total number of equally populated bins, given the smaller total number of stars in each stellar sub-group. As we did previously, we discarded the outermost bin because of the lack of circular symmetry due to the shape of the MUSE FOV, that could potentially bias the analysis. The results of the MP kinematic analysis are summarized in Fig. 11. In the top and bottom panels, we show the rotational velocity profiles obtained for SP and FP stars, respectively. As in Fig. 7, grey circles correspond to the MUSE data and open circles to the FLAMES data. We also show the best-fitting curve, obtained in the same way as for the total population. We should stress here that because of the lower number of radial bins and larger uncertainties, we decided to adopt the same value of $R_{pk}$ as obtained for the entire sample in the fitting procedure. The SP population shows the stronger rotation with a peak velocity $v_{pk} = 1.19^{+0.25}_{-0.14}$, while the FP rotates at a lower pace with $v_{pk} = 0.65^{+0.13}_{-0.12}$. The difference in rotation velocity between MPs is
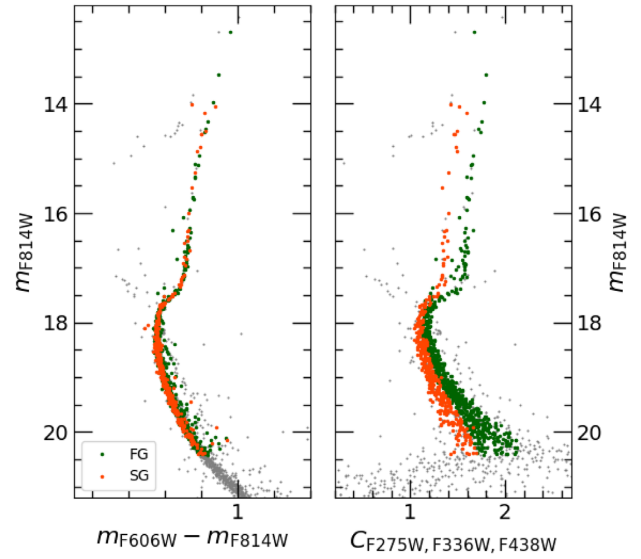


**Figure 10.** Left-hand panel: ($m_{F814W}$, $m_{F606W} - m_{F814W}$) CMD. Right-hand panel: ($m_{F814W}$, $C_{F275W, F336W, F438W} = (m_{F275W} - m_{F336W}) - (m_{F336W} - m_{F438W})$)) pseudo-CMD. In both panels, all the stars from the complete MUSE catalogue are shown as grey dots, while (quality selected, see Section 3) FP and SP stars are shown as green and orange dots, respectively.

significant at a $2.8\sigma$ level. The different binary fraction between FP and SP stars, which has been shown (Dalessandro et al. 2018a) to have an impact on the cluster kinematics at intermediate-large cluster-centric distances, is not expected to play a role on the differential rotation detected here (see also Hong et al. 2019). Also, we note that the slightly increasing profile (at $Log(R) > 2$) of $V_{rot}$ and $V_{rot}/\sigma$ discussed above seems to be driven mainly by the SP population.

Additional data are necessary to draw firmer conclusions concerning this feature and the possible differences in its significance in the SP and the FP populations. Further insight on these kinematic properties can provide key constraints on the dynamical evolution of multiple populations. Finally, we find that the average rotation axis angle of the two populations are $102° \pm 40°$ and $120° \pm 36°$ for the FP and SP, respectively, thus consistent with that of the total sample.

We matched the *HST* PM catalogue with the FP and SP stars to study their kinematic patterns also in the plane of the sky. We divided the two populations in three equally populated radial bins and we studied the radial and tangential components of the velocity dispersions. Results are shown in Fig. 12. The two populations show a very similar behaviour in terms of their radial components as expected for two sub-populations sharing the same radial distributions (Dalessandro et al. 2014). On the contrary, the SP shows a larger tangential dispersion than FP stars in the innermost bin that can be interpreted as evidence on the plane of the sky of a larger rotation, in agreement with the difference in the rotation profile found with the MUSE data.

The observed MP 3D kinematic results are generally consistent with a formation scenario in which a second population formed from the ejecta of a rotating first population (see e.g. Bekki 2010, 2011). These results are also in qualitative agreement with the studies of M 13 by Cordero et al. (2017) and M 80 by Kamann et al. (2020), who also found a higher rotation velocity for the SP sub-population.

## 6 SUMMARY AND DISCUSSION

The high-resolution 3D kinematic analysis presented in this paper has revealed for the first time a significant rotation signal in the
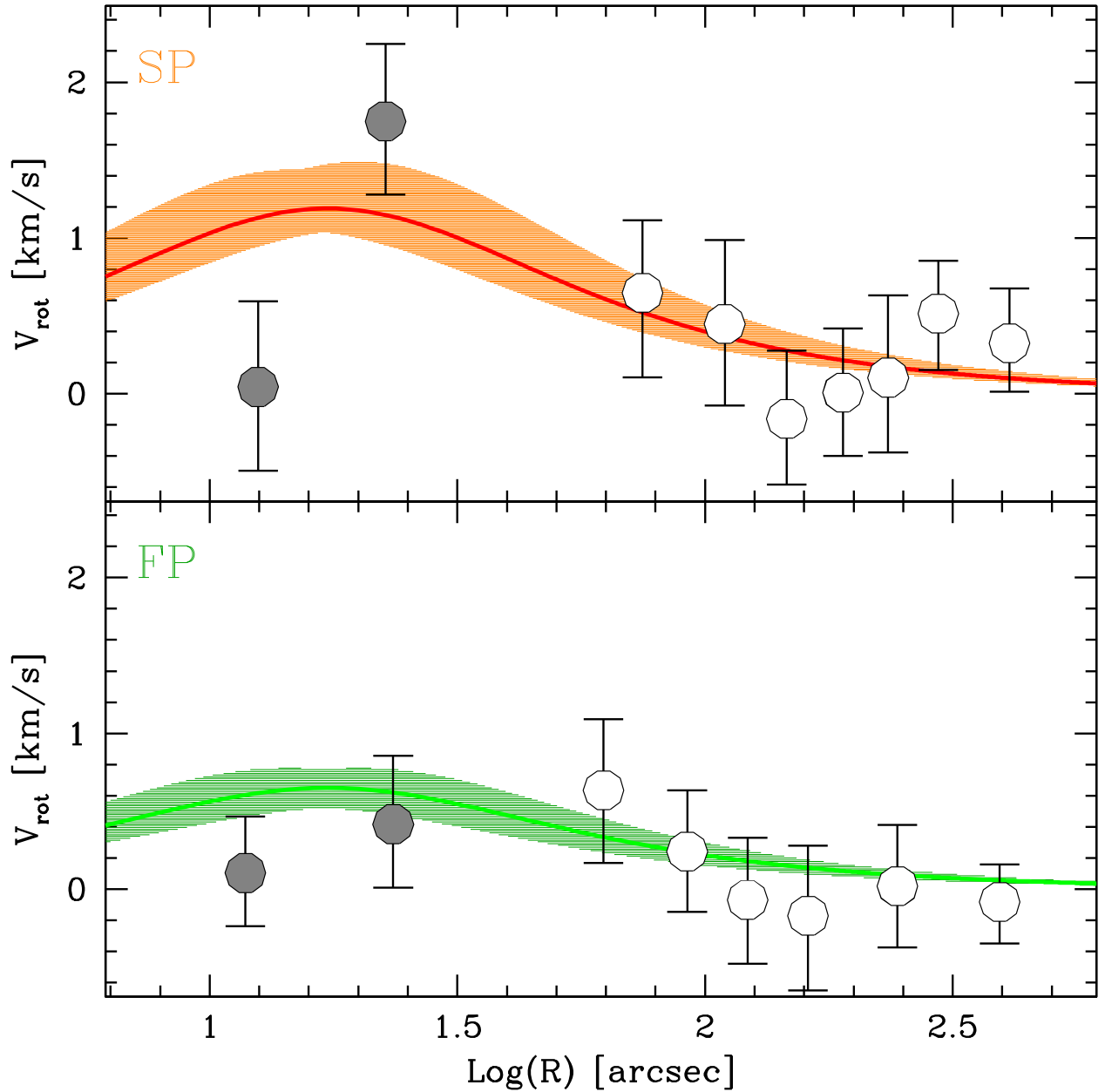
**Figure 11.** Rotational velocity profiles from MUSE and FLAMES data for FP and SP stars (top and bottom panels, respectively). We also show the best-fitting curves (see text for details about the fit) and relative errors.

innermost regions ($R < 30$ arcsec) of NGC 6362. The rotation curve shows a velocity peak $v_{pk} \sim 1$ km s$^{-1}$ at $R_{pk} \sim 20$ arcsec roughly corresponding to 0.1 $R_h$, then the rotation signal rapidly declines and totally disappears for $R > 100$ arcsec. Such a central rotation peak is a rare feature in GCs, with the only comparable case being M 15 (e.g. van den Bosch et al. 2006). However, it is worth stressing that at odds with NGC 6362, M 15 is a post-core collapse cluster and the observed peculiar rotation patterns can be due to recent physical events like cluster oscillations (see for example Usher et al. (2021).

Based on results from *N*-body simulations (Tiongco et al. 2017), a very central rotation peak ($R_{pk} < R_h$) is expected only in very dynamically evolved star clusters that lost a significant amount of their mass because of both two-body relaxation effects and interaction with the host galaxy potential. In fact, in rotating stellar clusters, the peak of the rotation curve is expected to be located

between 1 and 2 $R_h$ during the first stages of the cluster's evolution and then to gradually move inward in the very advanced dynamical phases.

Rotation is also expected to become weaker as the system evolves and loses mass and the current observed rotation is therefore only the remnant of a stronger primordial one. Indeed, assuming that NGC 6362 lost 50 per cent$-$80 per cent of its initial mass as constrained by its MP radial distributions (Dalessandro et al. 2014), the simulations presented in Tiongco et al. (2017) would suggest the initial rotation could have been 5–10 times larger than the current one.

While the observed values of both $R_{pk}$ and $v_{pk}$ are in general qualitative agreement with the expected dynamical evolution for a star cluster, the value of the peak of $V_{rot}/\sigma$ we find ($\sim$0.3; see Fig. 7) is larger by a factor of about 5 than the value suggested by simulations for clusters in the advanced stages of their evolution like NGC 6362.
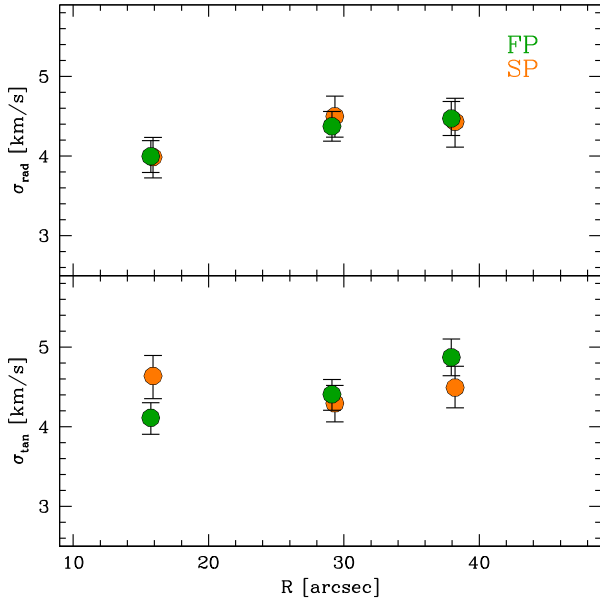
**Figure 12.** From top to bottom: radial and tangential velocity dispersion profiles in the plane of the sky, obtained from PM, for FP and SP stars (green and orange symbols, respectively).

The derived values $v_{pk}/\sigma$ and the location of $R_{pk}$ possibly suggest that NGC 6362 formed with initial conditions characterized by a high rotation and/or that internal dynamical processes may have been able to preserve the cluster central rotation for a long time-scale. Additional simulations will be needed to understand the range of initial kinematic properties and the dynamical ingredients required to explain such a high value of the peak of $V_{rot}/\sigma$ in the late stages of a cluster's evolution.

We can in principle exclude that the very different binary fraction between FP and SP sub-populations is playing a role, as they are expected to manifest their effects at intermediate-large distances from the cluster centre (Dalessandro et al. 2018a; Hong et al. 2019). It might be interesting to consider that MPs, which were likely born with different primordial structural and kinematic patterns, contribute in different ways to the overall energy budget of the cluster. In this context, it is worth emphasising that in NGC 6362 the SP sub-population is actually dominating the total rotation signal in the innermost region and recent observations (Cordero et al. 2017; Kamann et al. 2020) suggesting this might actually be a common behaviour.

Further investigations both from the observational and theoretical point of view are certainly needed to shed light on both the formation of GCs and their MPs and how the co-existence of sub-populations of stars with different initial kinematic properties may impact our understanding of the kinematics and structure of present-day star clusters. The simplicity of GCs is certainly a concept of the past, and while unprecedented observations unveils more and more details, theoretical models accounting for both kinematical and chemical complexities of GC stellar populations become more and more important.

## DATA AVAILABILITY

The raw MUSE data are available from the ESO archive (https://archive.eso.org/eso/eso_archive_main.html). Detailed results obtained in this work are available from the authors upon reasonable request.

## REFERENCES

Anderson J., King I. R., 2003, AJ, 126, 772
Bastian N., Lardo C., 2018, ARA&A, 56, 83
Bastian N., Lamers H. J. G. L. M., de Mink S. E., Longmore S. N., Goodwin S. P., Geiles M., 2013, MNRAS, 436, 2398
Baumgardt H., Hilker M., Sollima A., Bellini A., 2019, MNRAS, 482, 5138
Bekki K., 2010, ApJ, 724, L99
Bekki K., 2011, MNRAS, 412, 2241
Bellazzini M., Bragaglia A., Carretta E., Gratton R. G., Lucatello S., Catanzaro G., Leone F., 2012, A&A, 538, A18
Bellini A. et al., 2014, ApJ, 797, 115
Bellini A. et al., 2015, ApJ, 810, L13
Bellini A. et al., 2018, ApJ, 853, 86
Bianchini P., van der Marel R. P., del Pino A., Watkins L. L., Bellini A., Fardal M. A., Libralato M., Sills A., 2018, MNRAS, 481, 2125
Breen P. G., Varri A. L., Heggie D. C., 2017, MNRAS, 471, 2778
Brodie J. P., Strader J., 2006, ARA&A, 44, 193
Calura F., D'Ercole A., Vesperini E., Vanzella E., Sollima A., 2019, MNRAS, 489, 3269
Cassisi S., Salaris M., 2013, Old Stellar Populations: How to Study the Fossil Record of Galaxy Formation. Wiley-VCH, Weinheim, Germany, p. 538
Chandrasekhar S., 1969, ApJ, 157, 1419
Copin Y. et al., 2001, in Combes F., Barret D., Thévenin F., eds, SF2A-2001: Semaine De L'astrophysique Francaise. EdP-Sciences, Lyon, France, p. 289
Cordero M. J., Hénault-Brunet V., Pilachowski C. A., Balbinot E., Johnson C. I., Varri A. L., 2017, MNRAS, 465, 3515
D'Ercole A., Vesperini E., D'Antona F., McMillan S. L. W., Recchi S., 2008, MNRAS, 391, 825
Dalessandro E., Schiavon R. P., Rood R. T., Ferraro F. R., Sohn S. T., Lanzoni B., O'Connell R. W., 2012, AJ, 144, 126
Dalessandro E. et al., 2014, ApJ, 791, L4
Dalessandro E., Lapenna E., Mucciarelli A., Origlia L., Ferraro F. R., Lanzoni B., 2016, ApJ, 829, 77
Dalessandro E. et al., 2018a, ApJ, 864, 33
Dalessandro E. et al., 2018b, ApJ, 859, 15
Dalessandro E. et al., 2019, ApJ, 884, L24
Dalessandro E. et al., 2021, ApJ, 909, 90
Decressin T., Charbonnel C., Meynet G., 2007, A&A, 475, 859
Denissenkov P. A., Hartwick F. D. A., 2014, MNRAS, 437, L21
Dotter A. et al., 2010, ApJ, 708, 698
Einsel C., Spurzem R., 1999, MNRAS, 302, 81
Ernst A., Glaschke P., Fiestas J., Just A., Spurzem R., 2007, MNRAS, 377, 465
Fabricius M. H. et al., 2014, ApJ, 787, L26
Ferraro F. R. et al., 2018, ApJ, 860, 50
Forbes D. A. et al., 2018, Proc. R. Soc. A, 474, 20170616
Foreman-Mackey D., Hogg D. W., Lang D., Goodman J., 2013, PASP, 125, 306

Gieles M. et al., 2018, MNRAS, 478, 2461

Gratton R., Bragaglia A., Carretta E., D'Orazi V., Lucatello S., Sollima A., 2019, A&AR, 27, 8

Harris W. E., 1996, AJ, 112, 1487 2010 edition

Hénault-Brunet V. et al., 2012, A&A, 545, L1

Hénault-Brunet V., Gieles M., Agertz O., Read J. I., 2015, MNRAS, 450, 1164

Hong J., Kim E., Lee H. M., Spurzem R., 2013, MNRAS, 430, 2960

Hong J., Patel S., Vesperini E., Webb J., Dalessandro E., 2019, MNRAS, 483, 2592

Husser T.-O., Wende-von Berg S., Dreizler S., Homeier D., Reiners A., Barman T., Hauschildt P. H., 2013, A&A, 553, A6

Husser T.-O. et al., 2016, A&A, 588, A148

Kamann S., 2018, Astrophysics Source Code Library, record ascl:1805.021

Kamann S., Wisotzki L., Roth M. M., 2013, A&A, 549, A71

Kamann S. et al., 2018a, MNRAS, 473, 5591

Kamann S. et al., 2018b, MNRAS, 480, 1689

Kamann S. et al., 2020, MNRAS, 492, 966

Krajnović D., Cappellari M., de Zeeuw P. T., Copin Y., 2006, MNRAS, 366, 787

Krumholz M. R., McKee C. F., Bland-Hawthorn J., 2019, ARA&A, 57, 227

Kundu R., Fernández-Trincado J. G., Minniti D., Singh H. P., Moreno E., Reylé C., Robin A. C., Soto M., 2019, MNRAS, 489, 4565

Lanzoni B. et al., 2018a, ApJ, 861, 16

Lanzoni B. et al., 2018b, ApJ, 865, 11

Lynden-Bell D., 1967, MNRAS, 136, 101

Mackey A. D., Da Costa G. S., Ferguson A. M. N., Yong D., 2013, ApJ, 762, 65

Mapelli M., 2017, MNRAS, 467, 3255

Massari D., Lapenna E., Bragaglia A., Dalessandro E., Rodrigo C. R., Amigo P., 2016, MNRAS, 458, 4162

Massari D. et al., 2017, MNRAS, 468, 1249

Mastrobuono-Battisti A., Perets H. B., 2013, ApJ, 779, 85

Miholics M., Webb J. J., Sills A., 2015, MNRAS, 454, 2166

Milone A. P. et al., 2017, MNRAS, 464, 3636

Milone A. P. et al., 2020, MNRAS, 492, 5457

Mucciarelli A. et al., 2016, ApJ, 824, 73

Nardiello D. et al., 2018, MNRAS, 481, 3382

Neumayer N., Seth A., Böker T., 2020, A&AR, 28, 4

Nguyen D. D. et al., 2018, ApJ, 858, 118

Paust N. E. Q. et al., 2010, AJ, 139, 476

Pietrinferni A., Cassisi S., Salaris M., Castelli F., 2006, ApJ, 642, 797

Piotto G. et al., 2015, AJ, 149, 91

Pryor C., Meylan G., 1993, Structure and Dynamics of Globular Clusters. Astron. Soc. Pac., San Francisco, p. 357

Raso S. et al., 2020, ApJ, 895, 15

Richer H. B. et al., 2013, ApJ, 771, L15

Sbordone L., Salaris M., Weiss A., Cassisi S., 2011, A&A, 534, A9

Sollima A., Baumgardt H., Hilker M., 2019, MNRAS, 485, 1460

Tiongco M. A., Vesperini E., Varri A. L., 2016, MNRAS, 461, 402

Tiongco M. A., Vesperini E., Varri A. L., 2017, MNRAS, 469, 683

Tiongco M. A., Vesperini E., Varri A. L., 2019, MNRAS, 487, 5535

Tonry J., Davis M., 1979, AJ, 84, 1511

Usher C., Kamann S., Gieles M., Hénault-Brunet V., Dalessandro E., Balbinot E., Sollima A., 2021, MNRAS, 503, 1680

van den Bergh S., 2008, AJ, 135, 1731

van den Bosch R., de Zeeuw T., Gebhardt K., Noyola E., van de Van G, 2006, ApJ, 641, 852

Vesperini E., McMillan S. L. W., D'Antona F., D'Ercole A., 2013, MNRAS, 429, 1913

Watkins L. L., van der Marel R. P., Bellini A., Anderson J., 2015, ApJ, 803, 29

Weilbacher P. M. et al., 2020, A&A, 641, A28

This paper has been typeset from a TeX/LaTeX file prepared by the author.